








Stress-strain engineering of single-crystalline silicon membranes by ion implantation: Towards direct-gap group-IV semiconductors

Mateus G. Masteghin ^{1,2} Vivian Tong ³ Eleanor B. Schneider ^{1,2} Cameron C. L. Underwood ¹ Tomas Peach ¹
Benedict N. Murdin,¹ Roger P. Webb ^{1,2} Steven K. Clowes,¹ and David C. Cox ^{1,2,3,*}

¹*Advanced Technology Institute, University of Surrey, Guildford GU2 7XH, United Kingdom*

²*Ion Beam Centre, University of Surrey, Guildford GU2 7XH, United Kingdom*

³*National Physical Laboratory, Teddington TW11 0LW, United Kingdom*



(Received 10 September 2021; accepted 30 November 2021; published 21 December 2021)

The introduction of strain into semiconductors offers a well-known route to modify their band structure. Here, we show a single-step procedure for generating such strains smoothly and deterministically, over a very wide range, using a simple, easily available, highly scalable, ion implantation technique to control the degree of amorphization in and around single-crystal membranes. The amorphization controls the density of the material and thus the tension in the neighboring crystalline regions. We have demonstrated up to 3.1% biaxial tensile strain and 8.5% uniaxial strain in silicon, based on micro-Raman spectroscopy. This method achieves strain levels never previously reached in mesoscopic defect-free, crystalline silicon structures. The flexible, gently controllable, single-step process points toward very high mobility complementary metal-oxide-semiconductor devices and easy fabrication of direct-bandgap germanium for silicon-compatible optoelectronics.

DOI: [10.1103/PhysRevMaterials.5.124603](https://doi.org/10.1103/PhysRevMaterials.5.124603)

I. INTRODUCTION

Strain can modify the bandgap nature of semiconductors, controlling the photoemission probability and gain [1–6]. Silicon-compatible direct bandgap semiconductors would produce a drastic improvement in optoelectronic/photonic devices due to the compatibility with the drive electronics in complementary metal-oxide-semiconductors (CMOSs) [7]. To have the silicon (Si) conduction band minimum at the gamma (Γ) point, a strain of 10–13% [8] is required. Although such high strain levels are difficult to achieve, smaller amounts are enough to improve the light emission efficiency by reducing the momentum required during transitions [9]. Furthermore, a transition from indirect to direct bandgap reportedly occurs at much lower strains in nanoscale silicon materials, for example, at 1–2% strain for hydrogen passivated silicon nanowire with 3.1 nm diameter [10]. The most conventional method used to produce strained silicon involves exploiting the mismatch between the silicon (5.431 Å) and germanium (5.658 Å) lattices [11]. Other methods encompass surface modification [10], oxide growth followed by undercut [12], or a bending apparatus [13]. Nevertheless, even using multiple lithography steps, the reported strains are generally <2%, though up to 4.5% uniaxial strain has been produced in undercut silicon nanowire [14]. In germanium (Ge), the indirect-to-direct transition occurs at a much lower strain (1.9% for biaxial and >4% for uniaxial [2]), and up to 5.9% uniaxial strain at 20 K has been demonstrated with laser occurring at 5.4% [6].

The effect of ion irradiation on the matter has been observed in several amorphous materials, e.g., silica (SiO₂) [15,16], silicon nitride (Si₃N₄) [17–20], or metals [21,22], and under different ion beam conditions such as low-energy helium (He⁺) [18] and gallium (Ga⁺) [17] or high-energy noble gases [15]. A well-known effect is the plastic deformation of insulator materials (e.g., SiO₂ [16] and Si₃N₄ [19]) under high-energy irradiation due to a thermal spike after the implantation, herein called ion beam hammering [15,16]. This phenomenon corresponds to the shrinking of the dimensions parallel to the ion beam incidence while the dimensions parallel to the surface dilate, taking place when the ion beam range is larger than the sample size and the average electronic energy loss is higher than the 0.60 keV nm⁻¹ threshold. In contrast, upward bending of Si₃N₄ cantilevers, corresponding to a contraction of the surface after high-dose (~10¹⁷ atom cm⁻²) and low-energy (30 keV) Ga⁺ implants, is attributed to the formation of a thin metallic layer on the surface [17]. In addition to these mesoscopic induced strains, ion implantation (30 keV boron into Si, at a dose of 10¹⁵ ions cm⁻²) followed by thermal processing (20 min at 1000 °C) can induce nanoscopic strain fields as a result of dislocation loops generated from the damage tracks [23]. Nevertheless, the experiments reported in the literature investigated only tensile or compressive stress induced on the implanted region rather than on the neighboring unimplanted area. Here, we report ion implantation used to deterministically strain a pristine crystalline material by modifying the exposed region adjacent to it.

In this paper, freestanding single-crystal silicon membranes, with 35 nm thickness but mesoscopic area of 131.5 × 131.5 μm², have been strain engineered using xenon (Xe⁺) and gallium (Ga⁺) ion implantation in the surroundings, i.e., without compromising the single-crystal nature of the area

*d.cox@surrey.ac.uk

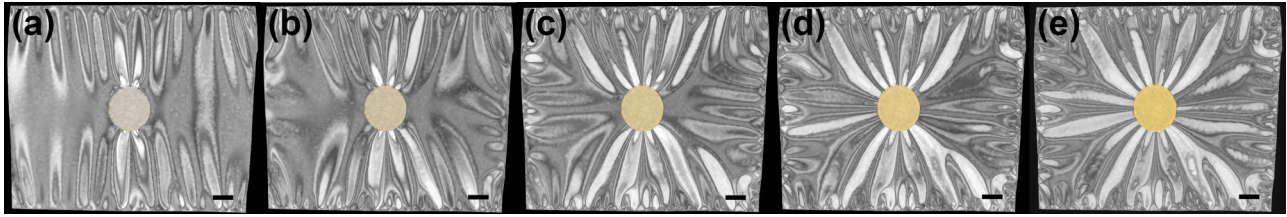


FIG. 1. Control of wrinkle symmetry. Scanning transmission electron microscopy (STEM) images showing the tensioning of the membrane. The contrast is produced by the single-crystal membrane angle relative to the electron beam and detector. A 25- μm -diameter circle was exposed to a 30 keV Xe^+ beam with 1.88×10^{14} ions $\text{cm}^{-2} \text{s}^{-1}$ for (a) 2 s, (b) 4 s, (c) 6 s, (d) 8 s, and (e) 10 s (the opacity of the false colored yellow indicates the irradiation duration). The scale bar corresponds to 10 μm .

being strained. The strain values were obtained using Raman spectroscopy. By controlling the implanted region around an unimplanted area of a single crystal, representing the place where an active device-region could be fabricated, we created strained membranes. This process is analogous to the tightening of a drum skin, and in what follows, we refer to the unexposed region of the window as the tympanum and the exposed region as the tensioner. We produced biaxial tension in tympana with circular patterns and uniaxial tension with high-aspect-ratio slot-shaped designs. We have also exploited the Si crystal anisotropy by altering the geometries of the slot-shaped tympana to optimize the achieved strain. Implanting at low energy, only the top surface is under tension, producing a bilayer material that tends to curl when freestanding or produces stress on neighboring materials when anchored. We discovered that the neighboring crystalline tympanum area is left flat and without shear based on electron backscatter diffraction (EBSD) measurements. The proposed method allowed us to reach up to 8.5% strain with very low implantation doses.

II. TENSIONING A BUCKLED SILICON THIN FILM

The membranes used in this paper were produced by back-etching a silicon-on-insulator (SOI) wafer to produce a square “window” in which only the top silicon (35 nm thick) device layer remains (see Appendix A for fabrication details). Implanting Xe^+ ions produce bond breaking of the silicon, and since amorphous silicon created by ion implantation has a higher density than crystalline silicon, the implanted area shrinks, producing tension. Most of the xenon evaporates, and in any case, the Xe concentration is small enough that it contributes negligible swelling. We note that, often ion implantation causes swelling rather than shrinkage, i.e., swelling in a-Si is associated with high-density implants, often of Si^+ , or with very low densities and creation of point defects, whereas shrinkage is associated with intermediate density implants [24–26], often by gaseous species, and amorphization damage rather than isolated defects. Nevertheless, since the 30 keV Xe^+ ion penetration depth calculated using the Surrey University Sputter Profile from Energy Deposition (SUSPRE) software [27,28] is shorter than the thickness of the silicon membrane (21 nm, i.e., approximately half of the total thickness), only the top implanted layer contracts followed by an upward bending in the case of a freestanding cantilever or a downward bowing when the exposed region is “clamped” at both sides. This occurs in a similar fashion to the bending of

a bimetallic thermocouple strip when submitted to a temperature change (see discussion below).

To illustrate the induced tension, we show the result of implanting circular spots of increasing dose in Fig. 1 (note this is the inverse of the tympanum structure described above). The wrinkles present in the membrane are due to the small unintentional compressive strain in the SOI [29], which is released when the window is fabricated. Increasing the Xe^+ dose gradually increases the silicon density in the exposed area, shrinking it, and causing tension in the neighboring unimplanted area. The images in Fig. 1 resemble a liquid droplet placed on a thin elastic membrane [30] in which its weight creates a downward bending (bowing) of the film underneath the droplet followed by the appearance of radial wrinkles. The analogy drawn between Fig. 1 and the downward bowing under the droplet not only supports the idea of bimaterial bending after the ion implantation (see Appendix C) but also emphasizes how gently and controllably the ion beam can induce strain. The evolution of wrinkles while increasing the ion dose is equivalent to different timeframes of the high-speed filming of the droplet falling into the floating thin film [31]. Therefore, this low-energy ion implantation-induced strain can be an excellent platform to study nanowrinkling patterns in freestanding thin films [32,33].

III. FLATTENING A BUCKLED SILICON MEMBRANE

Figure 2(a) shows a scanning transmission electron microscopy (STEM) image of an untreated membrane with obvious wrinkles. In Fig. 2(d), the blurriness and the bending of the higher-order transmission diffraction pattern (DP) of this membrane indicate that the wrinkles disturb any long-range order of the silicon crystal. To flatten the initially buckled Si membranes, Xe^+ ions were implanted as an annulus pattern, leaving a pristine circular tympanum at the center [Fig. 2(b)]. The effect of the ring amorphization on the central unexposed region is to introduce a tensile strain which causes the wrinkles in it to dissipate as the strain is increased from Fig. 2(b) to Fig. 2(c). The evolution of the wrinkles in the tympanum with increasing ion fluence in the tensioner can also be seen as a sharpening of the DP in Figs. 2(e)–2(f). Refer to the Supplemental Material for further information [34].

IV. STRAIN MEASUREMENT

Raman spectroscopy was employed to quantify the stress in each membrane by means of the Si peak shift. A 532 nm

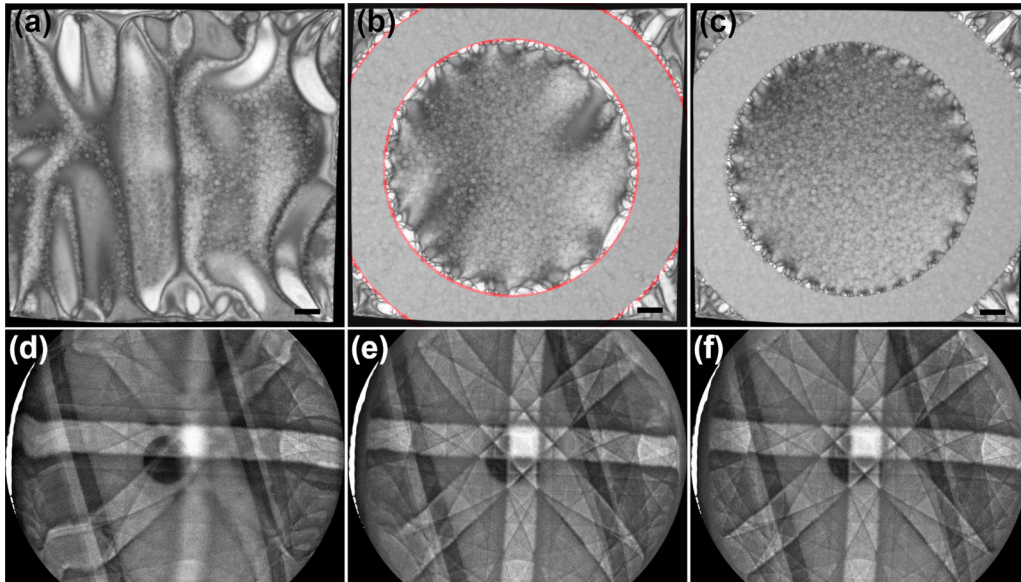


FIG. 2. Tightening a silicon drumskin. (a) Scanning transmission electron microscopy (STEM) image of an unexposed membrane with dimensions of $125 \times 125 \mu\text{m}^2$ like that in Fig. 1. (b) STEM image of the same membrane after exposing a $20\text{-}\mu\text{m}$ -wide annular tensioner ($140 \mu\text{m}$ outer diameter and $100 \mu\text{m}$ inner diameter indicated by the red lines) to 30 keV Xe^+ ions and a dose of $1.87 \times 10^{14} \text{ ions cm}^{-2}$. (c) The wrinkles are largely eliminated from the central tympanum, and there is now additional contrast between the amorphous and crystalline silicon after further exposing the same annulus doubling the total dose to $3.75 \times 10^{14} \text{ ions cm}^{-2}$. The electron diffraction patterns (DPs) in the 30 keV beam rocking mode shown in (d)–(f) correspond to a central $5\text{-}\mu\text{m}$ -diameter region of the membranes shown in (a)–(c), respectively. The DPs exhibit Kikuchi DPs characteristic of silicon (100). In (d), these lines are indistinct and bent, indicative of a scanned area that is lacking translational symmetry due to the wrinkles. In (e) and (f), these lines become more distinct, straight, and higher orders are visible, indicating that the scanned area becomes more and more translationally invariant (i.e., flat). Scale bars in (a)–(c) represent $10 \mu\text{m}$, and the maximum angle of the DP is 10.8° .

(2.33 eV) laser excitation energy with a $100\times$ objective lens ensured a spot size diameter of $3 \mu\text{m}$ with power below $100 \mu\text{W } \mu\text{m}^{-2}$ after attenuation filters, i.e., well below the level at which thermally induced shifts become important [35], even in nanocrystals embedded in a matrix with ~ 100 times smaller thermal conductivity than the crystalline silicon of the membranes here [36]. The laser excitation wavelength has an estimated penetration depth of $\sim 700 \text{ nm}$, ensuring that the strain is averaged across the entire thickness of the membrane [37]. The spectra were collected between 400 and 600 cm^{-1} . A spectral resolution of $1 \text{ cm}^{-1} \text{ pixel}^{-1}$ was achieved using $2400 \text{ lines mm}^{-1}$ grating. Before each measurement, a polystyrene sample located in a fixed focal length was used to perform internal autocalibration of the micro-Raman by means of matching the sharp and intense peak located at $1001.29 \pm 0.04 \text{ cm}^{-1}$, and a spectrum was collected from a piece of clean silicon (sonicated in acetone and oxygen plasma ash) to verify the overall setup precision on a nonstrained Si (T_{2g} peak at $520.98 \pm 0.02 \text{ cm}^{-1}$). Lorentzian functions were used to fit the peaks and quantify the resolution.

We investigated the degree of both biaxial and uniaxial strain produced by controlling the ratio of the areas of the tensioner to that of the tympanum. The magnitude of the strain was estimated from the shift of the T_{2g} mode in the Raman spectrum at $\omega_0 = 521 \text{ cm}^{-1}$. This shift can be found from the phonon deformation potentials [38–43]. For equibiaxial stress in the (100) plane and Raman scattering viewed perpendicular to this plane, $\Delta\omega = 2\omega_0 M_{(001)} \varepsilon / R$, where

$R^{-1} = [pS_{12} + q(S_{11} + S_{12})] / 2\omega_0^2$, p and q are the phonon deformation potentials, and S_{ij} are components of the compliance tensor. Using $p = -1.85 \omega_0^2$, $q = -2.31 \omega_0^2$ [39], $S_{11} = 7.68 \times 10^{-12} \text{ Pa}^{-1}$, and $S_{12} = -2.14 \times 10^{-12} \text{ Pa}^{-1}$ [39,41] produces $R = -226 \text{ GPa}$ (or $R/\omega_0 = -434 \text{ MPa/cm}^{-1}$). The equibiaxial modulus $M_{(001)} = 1/(S_{11} + S_{12}) = 181 \text{ GPa}$, so the conversion factor from the fractional Raman shift to the strain $\varepsilon = Q_{(001)} \Delta\omega / \omega_0$ is therefore $Q_{(001)} = R / 2M_{(001)} = -0.63$ (or $= \omega_0 / Q_{(001)} = 2\omega_0 M_{(001)} / R = -831 \text{ cm}^{-1}$). For uniaxial strain in (001), a similar relation applies $\Delta\omega = \omega_0 \varepsilon E / R$, where R is the same constant from above (and independent of direction), and the Young's modulus (E) is direction dependent. For uniaxial stress in the $[uv0]$ direction, $E_{[uv0]}^{-1} = E_{[100]}^{-1} + (E_{[110]}^{-1} - E_{[100]}^{-1}) \sin^2(2\varphi)$, where φ is the angle between the stress and $[100]$, $E_{[100]} = S_{11}^{-1} = 130 \text{ GPa}$, and $E_{[110]} = 4/(2S_{11} + 2S_{12} + S_{44}) = 168 \text{ GPa}$ (using $S_{44} = 12.7 \times 10^{-12} \text{ Pa}^{-1}$). The conversion factor from the fractional Raman shift to the strain is therefore $Q_{[uv0]} = R/E_{[uv0]}$, i.e., $Q_{[100]} = -1.74$, $Q_{[110]} = -1.34$ or $Q_{[120]} = -1.54$ (with corresponding $b = \omega_0 / Q = -300$, -387 , or -338 cm^{-1} , respectively). Although Fig. 1 implies out-of-plane bending of the exposed tensioner region, micro-Raman measurements were taken only in the tympanum, in the approximately flat areas (refer to Sec. V). We, therefore, neglect any modification to the conversion factors by curvature of the tympanum.

We note that there is some disagreement over the values of the phonon deformation potentials in the literature. Inferred values of R include -263 GPa [40], -262 GPa [42],

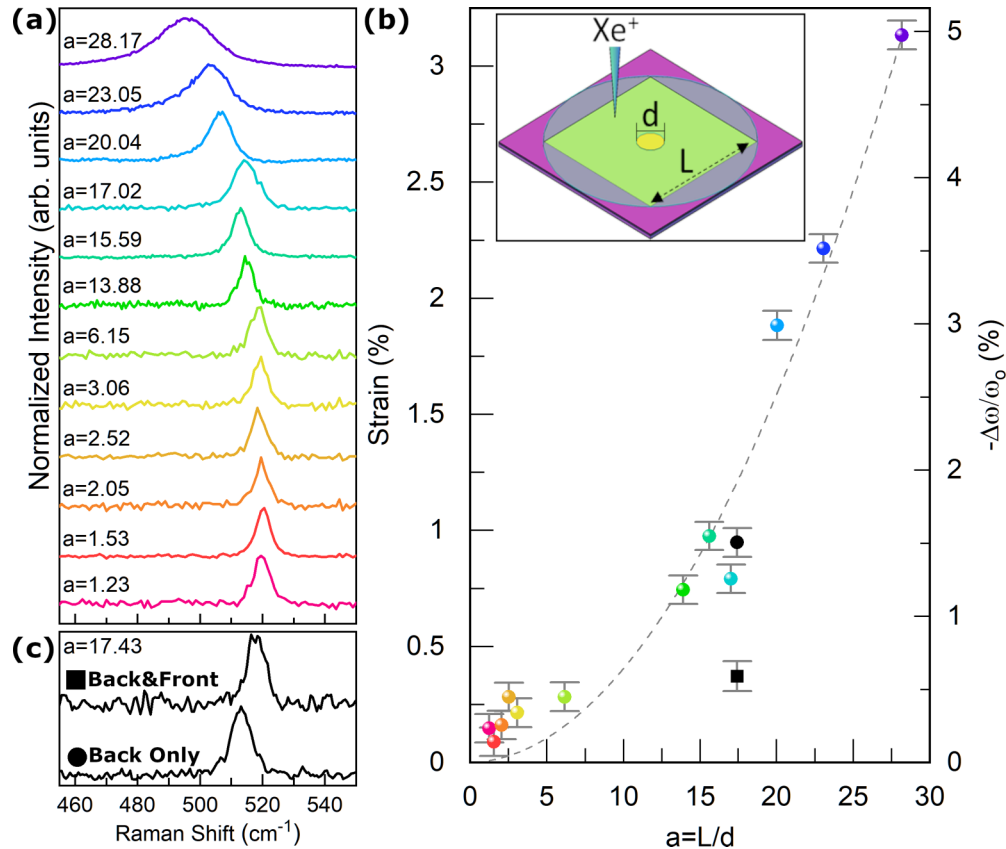


FIG. 3. Biaxial strain in circular tympana. (a) Raman spectra as a function of tympanum size relative to that of the surrounding exposure (tensioner). The Raman microscope laser spot size was $\sim 3 \mu\text{m}$, which is significantly smaller than the tympanum diameter. Spectra for different $a (= L/d)$ values are shown, in which the lowest a corresponds to the largest tympanum ($100 \mu\text{m}$ diameter) with the smallest strain, and the largest a and highest strain is obtained for the $5 \mu\text{m}$ tympanum diameter. The average window edge (L) = $131.5 \mu\text{m}$, and the tensioners were exposed to a 30 keV Xe^+ dose of $3.75 \times 10^{14} \text{ ions cm}^{-2}$. (b) Relationship between strain and the normalized size a , showing that largest tensioner to tympanum ratios result in highest values of strain, such as 3.1% for a $5\text{-}\mu\text{m}$ -diameter tympanum. The inset of (b) is a schematic drawing of the membranes used where purple indicates the region supported by the substrate, where the yellow circle in the center of the image corresponds to the unexposed tympanum, while the light-blue circle shows the tensioner region where Xe^+ were implanted (which overlaps with the edge of the window). Standard deviation error bars for strain values (%) were based on the micro-Raman spectral resolution and the uncertainty related to the Lorentz peak fit. (c) Raman spectra when the same membrane with $a = 17.43$ is exposed from the backside only (spectrum marked with a circle) followed by an opposite side exposure (marked with a square), in which the full amorphization caused a blue shift in the T_{2g} peak due to the unbending of the tensioner.

-255 GPa [43], and -247 GPa [44]. Using a larger magnitude of R would imply the strains produced in this paper are larger than we have inferred, but for interpretation of our experimental data, we keep the more conservative $R = -226 \text{ GPa}$ [39] to be sure not to overestimate the strain. We further note that, in germanium, it has been found that the conversion is nonlinear at high stress [45], and since the relationship obtained between ε and $\Delta\omega$ is sublinear, extrapolation from a small Raman shift would tend to overestimate the strain, but keeping a conservative value for R should mitigate any such effect, if present. Linearity in silicon has been confirmed up to 2.7% uniaxial strain [43].

A. Biaxial strain engineering

Figure 3(a) shows the evolution of the room-temperature Raman spectrum from the smallest area tensioner and largest tympanum, i.e., the least strain, up to the largest area tensioner and smallest tympanum, i.e., highest strain. The diameter of the circular tympanum was varied from $d = 100$ to $5 \mu\text{m}$, and

we introduced the parameter $a = L/d$ to normalize the data since the square membrane windows in which the circles have been produced do not all have the same dimensions, i.e., their edge sizes (L) range between 120 and $140 \mu\text{m}$. The inset of Fig. 3(c) illustrates the definition of these dimensions. At the lowest value of $a = L/d = 1.23$ ($d = 100 \mu\text{m}$), the tension is already enough to provide a flat tympanum. The highest value used $a = L/d = 128.17$ ($d = 5 \mu\text{m}$) was limited because, at this point, further reduction in d would approach the spatial resolution of our Raman microscope (which has Gaussian $1/e$ diameter $3 \mu\text{m}$, and 37% of the beam is outside this radius).

It is clear from Fig. 3(b) that the strain can be smoothly increased from small values up to very high biaxial strain. The increasing strain with a is a result of both membrane contraction and membrane bending after ion irradiation. To demonstrate that contraction alone is not responsible for the high strain values obtained, the same tensioner region has been exposed from the back and top sides to fully amorphize through the membrane and remove the bilayer structure.

Figure 3(c) shows that, after the second exposure (square data point), the strain in the tympanum decreases down to a very small number (blueshift) although still under tension. This proves that amorphization/contraction alone does not produce the observed strains obtained with ion irradiation on one side alone. We also acknowledge the fact that pure contraction should generate a higher planar shrinkage than a bending with constant Gaussian curvature, but due to the soft boundary between amorphized and crystalline regions, the curling mechanism is shown to be more complex (see Appendix C). Moreover, this backside exposure points to the possibility to induce strain while leaving the whole top surface pristine for devices. The fact that the Raman shift can be induced and then removed by treating first one side then the other shows that the origin of the Raman shift is not thermal (as does the fact that the Raman shift is smoothly controlled with changing of the dose, under nominally identical laser spot conditions). We note that the Raman spectrum broadens at high strain, and this is discussed in more detail below.

For STEM images of the membranes used in these experiments, refer to the Supplemental Material [34].

B. Uniaxial strain engineering

To investigate uniaxial strain and the ability to exploit the anisotropic Young's modulus, we produced tympana in high-aspect-ratio slot shapes. For such tympana, the stress and strain in the center is dominated by the uniaxial forces perpendicular to the long edges ([010]), with minor contribution from forces applied perpendicular to the short edges direction. However, when the aspect ratio is >4 , the stress on the rectangular tympana ends applied by the tensioner is smaller than the internal stress due to Poisson's ratio ($\nu \sim \frac{1}{4}$ for silicon), and we may treat the stress as uniaxial. Each tympanum has dimensions $50 \times 5 \mu\text{m}^2$, and the short axis, corresponding to the uniaxial stress, was oriented along [110], [120], or [010]. Therefore, the angles between the uniaxial stress directions and [100] are $\varphi = 45^\circ$, 67.5° , and 90° , respectively, corresponding to $\sin^2(2\varphi) = 1$, $\frac{1}{2}$, and 0, respectively. As the angle φ varies from 45° to 67.5° to 90° , the Raman shift varies from $\Delta\omega/\omega_0 = -0.013$ to -0.049 . Using the conversion factors derived above, we may calculate the uniaxial strains which correspond to $1.7 \pm 0.1\%$ to $2.6 \pm 0.1\%$ to $8.5 \pm 0.2\%$.

From above, $\Delta\omega/\omega_0 = \sigma/R$, where σ is the uniaxial stress, independent of the stress direction, and therefore, we would expect that, if the stress applied by the tensioner were constant and independent of orientation, a constant Raman shift would be observed. Evidently, the stress produced by the tensioner varies with angle and is largest for [010] and smallest for [110]. This finding points to the idea of exploiting the silicon anisotropy of the window to get the strongest tensioner force.

Peak asymmetry is characteristic of large uniaxial strain [14,46], and here, it could have additional effect from the asymmetric orientation of the high-aspect-ratio tympanum with ends approaching the finite-sized window edge which would be eliminated with larger membranes. This experiment also points out the lack of Raman artifacts on the measured strains, i.e., Raman laser heat dissipation should not change

with rectangular tympana orientation, and therefore, the shifts observed are not thermally induced.

V. INVESTIGATION OF STRAIN UNIFORMITY AND TYMPANUM FLATNESS

There is an observed increase of the full width at half maximum in Fig. 3(a) for high-stressed small tympana (17.9 cm^{-1} for the $5 \mu\text{m}$ circle, c.f. 5.1 cm^{-1} for the $100 \mu\text{m}$ circle) and also in Fig. 4 as the strain is increased either by controlling the rotation or the aspect ratio. This may be associated with increasing values of stress caused by curvature at the tympanum edges, dislocation nucleation caused by strain values beginning to approach the critical strain of silicon crystals (17%) [47], and the "tail effect" [48–50] of ion beam implants (the fact that the beam does not have a sharp edge) caused by scattered ions hitting the sample surface in a near-normal angle [51]. The Raman spot is also a Gaussian beam and has its own tail that overlaps with the lower dose implanted tympanum edge for small tympanum sizes (and the edges of the beam have lower intensity but larger area so can contribute substantially to the signal).

To investigate the flatness and crystallinity, we have used high angular resolution EBSD (HR-EBSD) on a strained tympanum with $a = 8.5$ ($20 \mu\text{m}$ diameter), experimental details of which can be found in Appendix B. EBSD DPs in Fig. 5(a) show the crystallinity of each region in the window. Region A is the strained crystalline Si membrane (the tympanum) used for cross-correlation analysis. Regions B–D show DPs from the surrounding pristine SOI crystal, the ion-implanted Si membrane (the tensioner), and ion-implanted SOI, respectively. These patterns were acquired at 15 kV electrons to decrease the probe depth since the elastic scattering mean free path for 20 kV electrons in Si is $\sim 17 \text{ nm}$ [52]. Regions C and D, which have ion-implanted top layers, show faint Kikuchi bands marked by the yellow dashed lines. The bands in region D show reversed contrast (dark bands on bright background, as opposed to bright bands on dark background as seen in region B). Contrast reversal is seen in patterns where diffraction contrast originates from the sample subsurface [52]. It is clear from region A in Fig. 5(a) that the unexposed part of the membrane remains highly crystalline.

To investigate the strain uniformity in the tympanum and its flatness, we mapped the deviatoric strain (i.e., the component of strain related to distortions away from hydrostatic) with respect to the center of the tympanum using the HR-EBSD. Figure 5(b) shows elastic strain and infinitesimal rotation components of the strained tympanum with respect to its center, using a DP from the center of the map as a strain reference. These data show the uniformity of elastic strain across the circular membrane but not the absolute strain nor the strain state with respect to the SOI. The strain state in the interior of the circular membrane is uniform up to the angular precision of the HR-EBSD dataset (1×10^{-3} radians, see methods in Appendix B), since angular precision in radians is numerically equal to the strain precision for small deflection angles. The measured ε_{12} and ε_{22} strain components appear higher than those without a component along the two axes. These are likely HR-EBSD calculation artifacts from slight

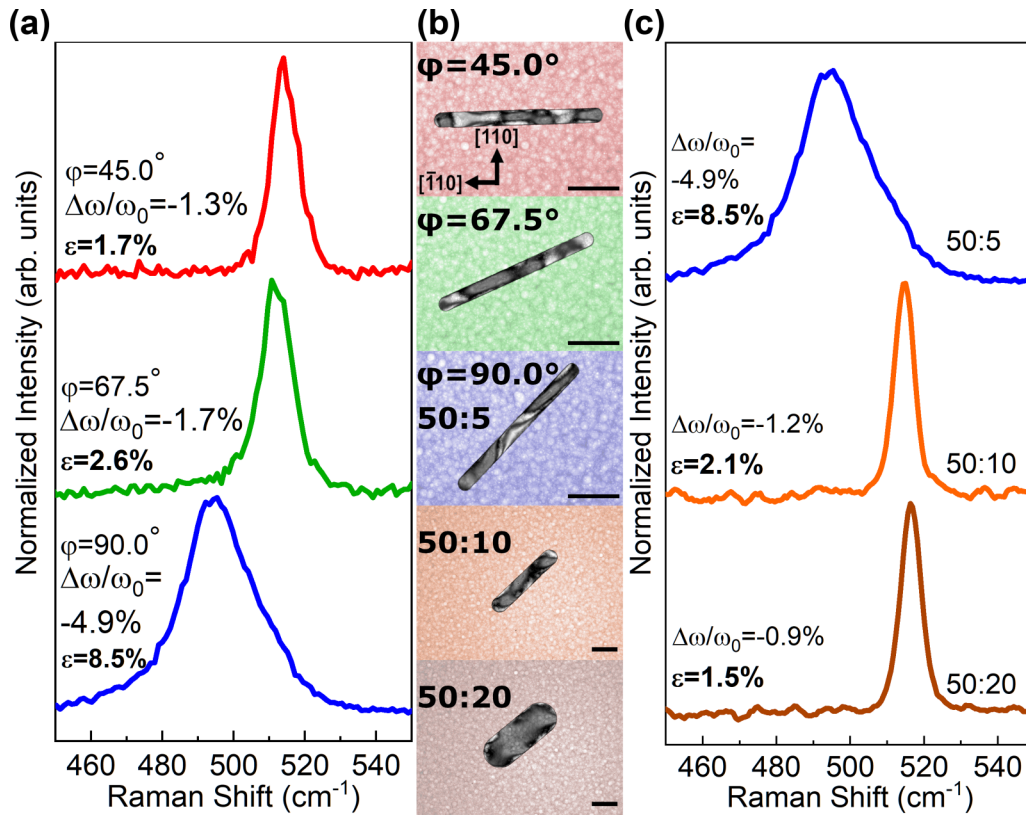


FIG. 4. Crystal orientation dependence of uniaxial tympanum strain. (a) Raman spectra obtained for rectangular tympana ($50 \times 5 \mu\text{m}^2$) with different crystallographic orientations shown in (b). The tympanum with short axis oriented in the $[010]$ direction ($\varphi = 90^\circ$) has the largest Raman shift and largest strain ($8.5 \pm 0.2\%$), whereas that with short axis oriented in the $[110]$ direction ($\varphi = 45^\circ$) has the smallest shift and strain ($1.7 \pm 0.1\%$). The $[120]$ tympanum ($\varphi = 67.5^\circ$) is intermediate ($2.6 \pm 0.1\%$ strain). Based on the redshift of the silicon T_{2g} peak, uniaxial strain values were inferred, indicated on each spectrum. Scale bars on the scanning transmission electron microscopy (STEM) images of (b) correspond to $15 \mu\text{m}$. (c) Rectangular tympanum width dependence showing that uniaxial strain increases as the width decreases, starting at $1.5 \pm 0.2\%$ for a $50 \times 20 \mu\text{m}^2$ tympanum and going through an intermediate strain value of $2.1 \pm 0.2\%$ for a $50 \times 10 \mu\text{m}^2$ tympanum. The labels indicate the dimensions of the tympana in micrometers. All samples in this figure had a 30 keV Xe^+ dose of $3.75 \times 10^{14} \text{ ions cm}^{-2}$.

wrinkles ($\sim 0.2^\circ$) on the tympanum surface, as evidenced by similar and reciprocal spatial features appearing in the out-of-plane strain and rotation components (HR-EBSD assumes a flat surface). Faint residual Kikuchi band features, visible in the ion-implanted regions, indicate that the tensioner is not fully amorphized through thickness but retains some crystallinity [regions C and D in Fig. 5(a)]. The strain distribution is relatively uniform across the membrane.

The infinitesimal rotation maps (ω_{12} , ω_{23} , and ω_{31}) and the kernel average misorientation map [see Appendix B] show that rotations in the center of the tympanum are negligible, but the tympanum circumference is bent slightly concave with a curvature of $0.2^\circ/\mu\text{m}$ ($0.1^\circ/\text{pixel}$) curvature. This indicates that the middle of the circular tympanum is essentially flat, and membrane rotations are localized to the tympanum edges.

The curvature detected at the edge of the tympanum is because the tensioner is curved. This curvature is allowed by take-up of the excess silicon evident as wrinkles in the unprocessed membrane (Figs. 1 and 2). Clearly, the distance from the window edge to the tympanum edge is reduced compared with the width the tensioner would have if it were flat, i.e., the bending contributes additional stress on the tympanum. The magnitude of this contribution is unclear, and further experiment/modeling is required to understand the mechanism fully,

such as using diffraction [48]. The bending at the tympanum edges also shows the extent of any depth dependence in the tympanum strain that could limit the usefulness for devices, which is therefore presumably limited to approximately the same $1 \mu\text{m}$ width ring around the tympanum edge. The curvature we observe in the center of the tympanum of Fig. 5(b) is negligible and no worse than often observed in epitaxially grown layers [53], though edge effects might become important at the highest strains, depending on the application. We note that EBSD can be used to measure strain, and a magnitude of several percent would be in many cases easy to detect. However, referencing to unstrained silicon is required for an absolute strain measurement, and in these samples, there is none on the surface (because the membrane outside the window is compressively strained, hence the wrinkles).

VI. CONCLUSIONS

A focused ion beam microscope was used to implant Xe^+ in a suspended single-crystal silicon membrane around circular and rectangular tympana with different orientations. It has been shown that the implantation induces bowing of the exposed region (tensioner), resulting initially in a stretching out of the wrinkled tympanum followed by its straining as the

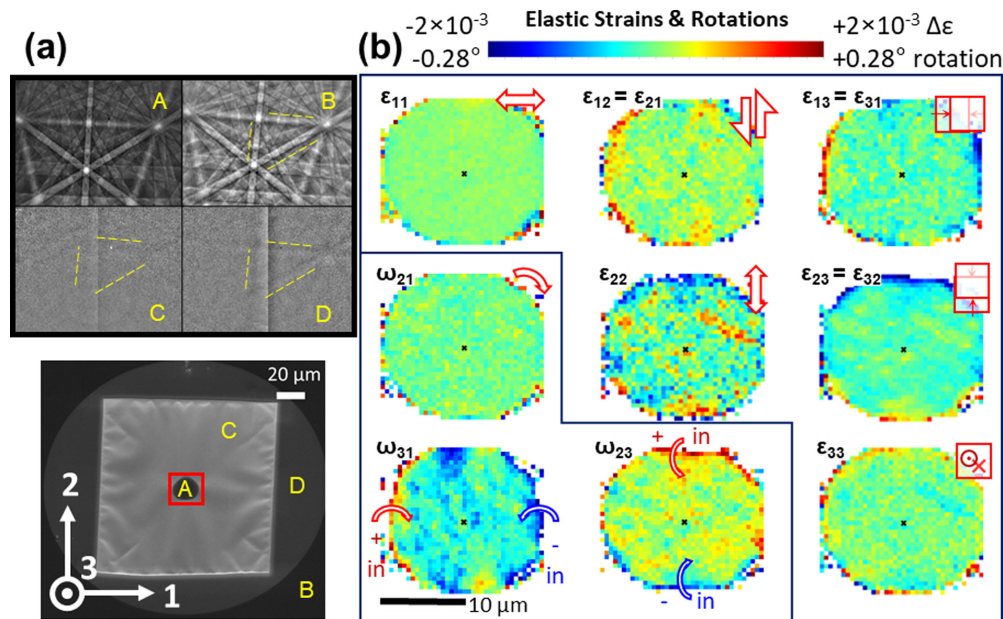


FIG. 5. Strain uniformity, bending orientation, and crystallinity maps of the strained tympanum. The circular tympanum of diameter $20 \mu\text{m}$ ($a = 8.5$) was produced with 30 keV Xe^+ and a dose of $3.75 \times 10^{14} \text{ ions cm}^{-2}$. (a) Example diffraction patterns from four regions of the sample: A = crystalline Si membrane forming the tympanum, used for high angular resolution electron backscatter diffraction (HR-EBSD) cross-correlation analysis; B = crystalline silicon-on-insulator (SOI); C = ion-implanted Si membrane forming the tensioner; D = ion-implanted SOI. Kikuchi bands are marked by the yellow dashed lines are obviously in unexposed (crystalline) materials and faint in exposed (amorphized) material. The bottom panel presents in-lens secondary electron image of the Si window with a $20 \mu\text{m}$ tympanum at the center. The HR-EBSD field of view is marked by the red box. (b) Maps showing deviation of the elastic strain and orientation obtained with the HR-EBSD across region A, the tympanum, relative to the center (marked with a black cross). Coordinate axes are marked in (a). The maps show high uniformity, with a very slight bowing visible from the in-plane shear strain components and in-plane rotation components.

dose increases. The strain and its uniformity were measured by Raman spectroscopy and EBSD, respectively. Either biaxial or uniaxial tensile strains can be induced by choice of the shape of the tympanum, up to 3.1 and 8.5%, correspondingly. Such high strain can be obtained in a relatively large active area exploring the silicon anisotropy. We recognize that the magnitude in the induced strain is indirectly measured via the Raman method; however, the strain measurements in this paper were calculated using conservative values for the phonon deformation potentials in the interpretation of the observed Raman shift. Using the most recent values [40] available would result in the maximum uniaxial strain achieved of 10%. A large flat area, with $\leq 0.1^\circ$ per μm membrane curvature in the outer $1 \mu\text{m}$, was observed in the biaxial-strained circular tympanum, although about 1° per μm curvature was observed in the direction of the short axis in a small uniaxial-strained rectangular tympanum. Such levels of strain are below fracture strengths of Si nanostructures at 293 K [54,55], and stress relaxation effect has not been observed.

Considering the wide interest in strained group-IV semiconductors for light emitters and photonic platforms [56], fast and scalable methods for strain incorporation are highly attractive. The strain uniformity across the membrane is one of the advantages of using ion implantation for strain generation to ensure a uniform bandgap energy. Moreover, the expected higher mobility of the strained crystal will prevent current flow via the implanted regions, and its narrower bandgap will concentrate carriers in those lower energy states, and therefore, improved optoelectronic properties are to be expected.

This technique induces biaxial or uniaxial tensile strain in thin films using a single-step procedure. Thus, if the same technique is applied to germanium membranes [57] with minor modification to the beam parameters, such as acceleration voltage and dose, as per the discussion in Appendix C, it would turn into a direct bandgap semiconductor with potential for many optical applications, e.g., lasers, due to its CMOS compatibility. The implications of this paper in photonics go beyond pure germanium and can be also applied to $\text{Si}_{1-x}\text{Ge}_x$ [58] and $\text{Ge}_{1-x}\text{Sn}_x$ [59,60] structures grown either on buried SiO_2 or Si wafers. The highest strains have been produced with the smallest tympana, and this reduces the active area available. However, usable strains are achievable even in larger tympana, and optical devices have been fabricated with only a few square micrometers [1], and direct bandgap Ge can be achieved with this technique in $40 \mu\text{m}^2$. While this demonstration of induced strain has been achieved using a focused ion beam, it could easily be a scalable technology via traditional lithographic techniques and broad area implantation.

ACKNOWLEDGMENTS

M.G.M. acknowledges financial support from Engineering and Physical Sciences Research Council (EPSRC; Grant Ref. 2116075) and the University of Surrey/Advanced Technology Institute via URS/ORS studentships. B.N.M. and S.K.C. acknowledge support from EPSRC (ADDRFSS Grant Ref. EP/M009564/1). We would like to acknowledge the assistance

of the Surrey Ion Beam Centre which is a part of the UK National Ion Beam Centre and supported by EPSRC (Grant Ref. NS/A000059/1).

M.G.M., T.P., S.K.C., and D.C.C. conceptualized the work; M.G.M., V.T., and D.C.C. conducted the experiments, the investigation, and wrote the original draft; E.B.S., C.L.U., R.P.W., and S.K.C. assisted with software and codes; B.N.M. conducted the formal analysis of the model. All authors contributed to the review process.

APPENDIX A: MEMBRANE FABRICATION, ION IMPLANTATION, AND IMAGING METHODOLOGY

The top (100) silicon layer was thinned until 35 nm using reactive ion etching [61]. The bottom silicon was wet etched using a potassium hydroxide (KOH) solution, and the silicon dioxide layer was stripped using hydrofluoric acid [62,63]. The anisotropic wet etching of silicon by KOH resulted in silicon membrane windows of $\sim 131.5 \times 131.5 \mu\text{m}^2$ in which the directions along the edges are [110] and the diagonals of the squares are aligned to the [100] directions. A schematic drawing of the grid of the membranes and its crystal directions are depicted in Fig. 6.

For the xenon (Xe^+) ion implantation, a Dual Beam Microscope (FIB-SEM), Tescan FERA3, was used. An inductively coupled plasma source generates a Xe^+ ion beam by ionizing the xenon gas after interactions with free electrons at the cathode. An acceleration voltage of 30 keV was fixed by the anode, and a specimen current of 150 pA was maintained constant during the implantations by controlling the condenser lens voltage. The spot size while operating the microscope at these conditions was measured to be ~ 500 nm. Gallium (Ga^+) ion implantation was carried out in another FIB-SEM, FEI Nova Nanolab, in which the Ga^+ beam was generated by a liquid metal ion source. Acceleration voltages of 10, 20, and 30 keV were used, and the current was kept at 10 pA during the ion implantation, resulting in spot sizes of ~ 50 , 20, and 10 nm, respectively. The exposure patterns were produced within the FIB-SEM software interface and consisted of a simple circle, an annular pattern with inner and outer circle diameters, and a circle (circular tympanum) or rectangle with filleted edges (rectangular tympanum) subtracted from a square. Regardless of the design, the beam was scanned from the central part (circle center or a point in the inner shape boundary) toward the outer contour in a clockwise course, with a pitch size of 10 nm and a dwell time (in seconds) calculated based on $[DA(1.6 \times 10^{-19})]/Ni$, where D is the ion dose (or fluence) in ions per square centimeter, A is the exposed area in square centimeters, N is the number of points in the pattern (based on the area and $x - y$ pitch size), and i is the beam current measured in a Faraday cup using a Keithley Series 6400 Picoammeter.

SUSPRE software [28] is a Boltzmann transport solver based on the Projected Range ALgorithm (PRAL) that allows calculation of ion range, damage, and implant accumulation [64,65]. SUSPRE advantages include fast processing time with accurate determination of ion range when compared with SRIM. For further information about SUSPRE software, please refer to Ref. [27].

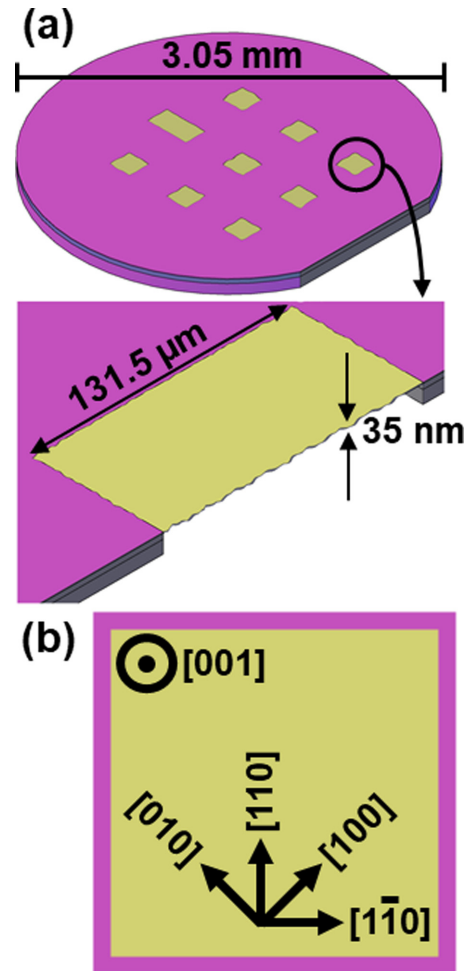


FIG. 6. Schematic drawing showing (a) grid and membrane dimensions and (b) crystallographic directions. 3.05 mm corresponds to standard transmission electron microscope (TEM) grid size, while window dimensions and crystal directions are a result of the anisotropic wet etching of silicon-on-insulator (SOI) wafers.

To monitor the changes on the membranes after implantation events, a 30 keV electron beam with spot size equal to 3.6 nm was used (beam current = 0.20 nA). Images were captured using the retractable STEM detector either using bright field or high angle annular dark field modes. The DPs were obtained using the same STEM detector with the electron beam in the rocking mode, in which the electron beam is rocked by the scanning coils at different angles to the normal to the same spot at the sample surface. In this mode, there is no focus of the beam between the scanning coils and the sample, while in normal imaging mode, a crossover point occurs at the objective lenses.

APPENDIX B: INVESTIGATION OF STRAIN UNIFORMITY AND RECTANGULAR TYMPANUM FLATNESS

EBSM maps were acquired on a Zeiss Auriga field emission SEM using an Oxford Instruments Nordlys F detector. The sample was mounted on a 70° pretilted stage, and the

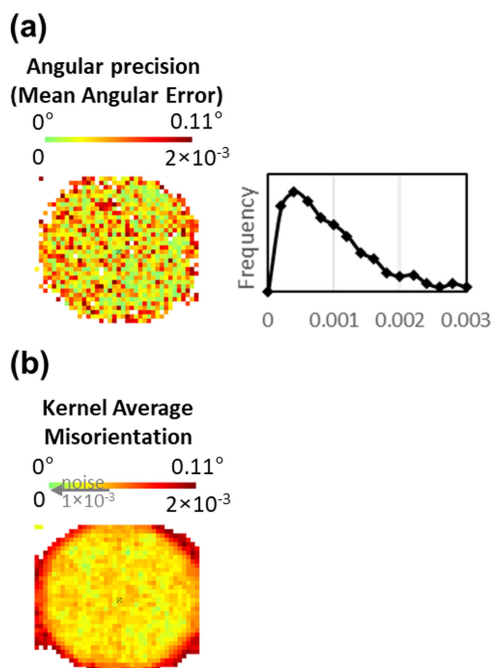


FIG. 7. (a) Left panel displays the mean angular error map, while the right panel shows the angular precision frequency distribution (histogram). The plots demonstrate how precisely the raw high angular resolution electron backscatter diffraction (HR-EBSD) measurements match the best-fit strains/rotations. From the histogram, the angular resolution of the data is $\sim 1 \times 10^{-3}$ radians. (b) HR-EBSD kernel average misorientation map showing that rotation between each point and its 4 nearest neighbors is negligible (within measurement noise) near the center of the circle. Short-range rotations could indicate nucleation of dislocation. Color bars correspond to rotations in degrees and radians.

working distance was 12.3 mm. The SEM was set at an accelerating voltage of 20 kV and ~ 10 nA probe current ($120 \mu\text{m}$

aperture with “High Current” mode). EBSD patterns were acquired at 640×480 pixels resolution with 700 ms exposure time. A background correction was applied to enhance band contrast. The map step size was $0.5 \mu\text{m}$. HR-EBSD analysis to calculate membrane rotations and in-plane elastic strain distributions was performed on CrossCourt 4 (BLG Vantage) using the methods in Ref. [66]. Pattern shifts were measured from cross-correlation of 50 regions of interest (128×128 pixels) per EBSD pattern. HR-EBSD dataset has an angular precision of 1×10^{-3} radians as per Fig. 7(a), and kernel average misorientation map in Fig. 7(b) complements Sec. V discussion.

The EBSD analysis covered the tip (red rectangle) of the $50\text{-}\mu\text{m}$ -long slot shown in Fig. 8(a). Figure 8(b) shows misorientation angle and axis relative to the center of the map. The membrane forms a saddle shape, bowing inward across the slot width and outward around the short edge. As for the circular tympana, only out-of-plane rotations are observed, meaning that there is no in-plane (twist) component. The Si window can be approximately described as a thin elastic membrane pinned on four edges bent by a curvature determined by a 0.1% [as per Eq. (C1) and $\kappa \approx \frac{3\Delta}{2t}$, discussed in Appendix C] linear misfit strain between the amorphized top layer and the crystalline bottom layer. Since the tensioner length is larger along the rectangular tympanum width than the slot length, a higher total bending moment is expected across the slot width than along the slot length. If the ratio between these bending moments exceeds the Poisson ratio of silicon (~ 0.25), the stretched tympanum shape turns from a concave bowl shape into a saddle shape. Thus, the membrane shape transitions from bowl shaped to saddle shaped as the sample aspect ratio increases from circular to slot shaped. This simple model further supports the bimaterial bending hypothesis. It is noteworthy that the ion-implantation method to strain membranes can gently achieve high strain levels in a $250 \mu\text{m}^2$ active region with $< 1.1 \pm 0.2^\circ$ rotation across the tympanum width at the center of the active region.

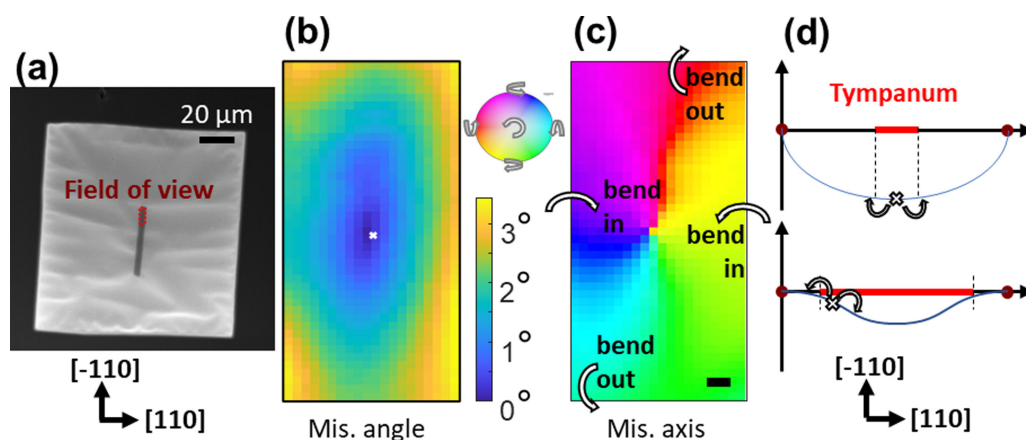


FIG. 8. (a) Scanning electron microscopy (SEM) image of the silicon-on-insulator (SOI) window and Si membrane containing a rectangular $50 \times 5 \mu\text{m}$ tympanum. The electron backscatter diffraction (EBSD) field of view is $3.8 \times 8.4 \mu\text{m}$ and indicated by the red dashed box. (b) EBSD misorientation angle map relative to the pixel at the center of the field of view, marked by the white cross. (c) Misorientation axis plots right-handed rotations about the axis according to the circular color key, which is plotted in the same coordinate frame as the EBSD map (white arrows indicate the direction of crystal rotation). The scale bar corresponds to 500 nm . (d) A schematic drawing of the membrane rotations in the saddle shaped tympanum. The white crosses indicate the EBSD field of view location in the schematic. Please note that the bending is exaggerated in the drawing for visualization purposes. The red section length corresponds to the tympanum width ($5 \mu\text{m}$) in the upper image and the tympanum length ($50 \mu\text{m}$) in the bottom image.

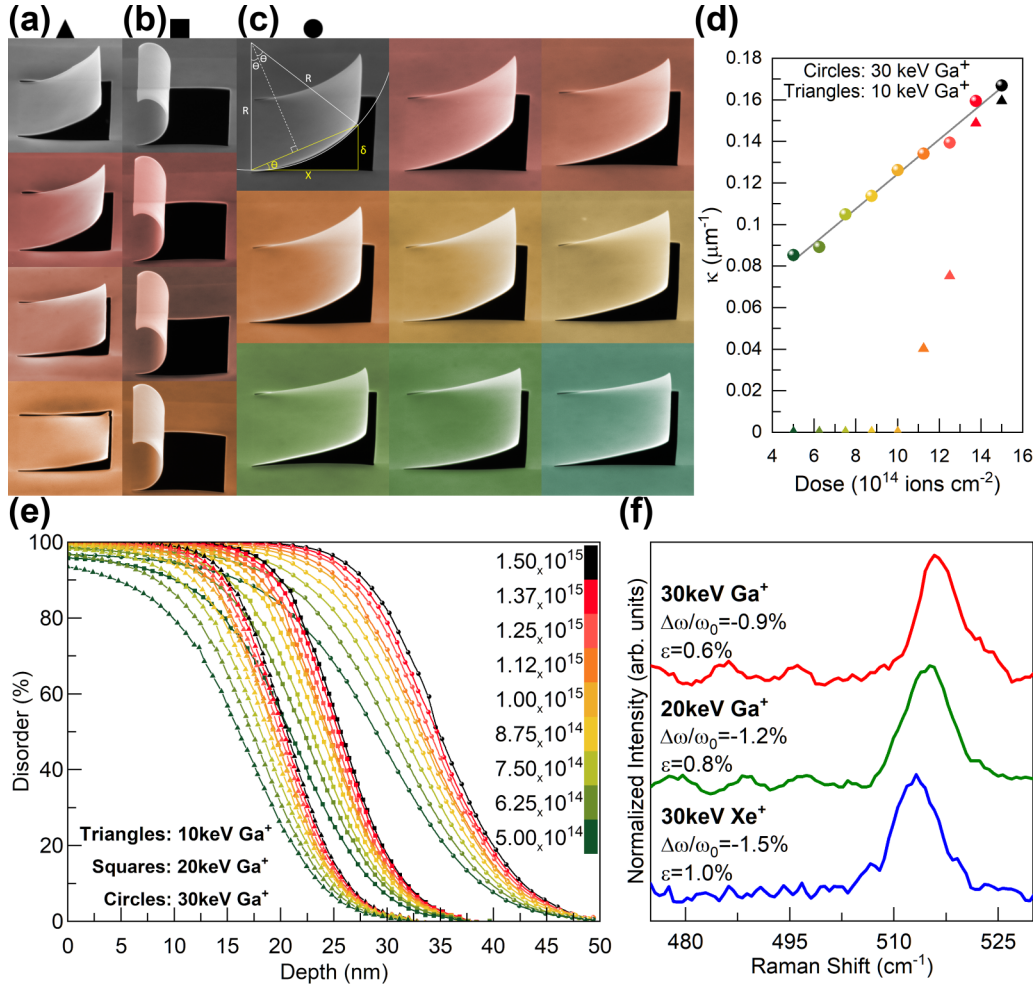


FIG. 9. Dependence of cantilever curvature on ion beam parameters. (a) Scanning electron microscopy (SEM) images of the cantilevers produced by (a) 10 keV Ga^+ , (b) 20 keV Ga^+ , and (c) 30 keV Ga^+ , in which the overlay colors correspond to the same doses depicted in (d), and fields of view are $6.5 \mu\text{m}$. (d) Graph of the inverse radius of curvature κ as a function of dose D for two different Ga^+ beam energies. (e) Disorder vs depth for the different energies and doses used in the experiments. The ordinate shows the fraction of host atoms that have been displaced by implant ions calculated using the SUSPRE model. Note that different points represent the implantation energies and colors correspond to different doses. (f) Raman spectra for circular tympana with tensioners implanted with 30 keV Xe^+ (blue), 20 keV Ga^+ (green), or 30 keV Ga^+ (red), corresponding to strains of 1.0, 0.8, and 0.6%, respectively. The three tympana all had the same diameter, $8 \mu\text{m}$ ($a = 17.5$) and $D = 5.00 \times 10^{14}$ ions cm^{-2} were used for Ga^+ implants, and $D = 3.75 \times 10^{14}$ ions cm^{-2} for Xe^+ implants. The difference in dosing is due to the higher onset of amorphization when Si is implanted with gallium as determined by SUSPRE.

APPENDIX C: GENERATING A BILAYER MATERIAL AND ITS STRAIN

We have investigated the mechanism for the tensile strain generation by the tensioner. The bimaterial generated after ion implantation/amorphization of the top layer and the resulting bending have been mentioned earlier.

Bimaterial bending is described by an equation like Timoshenko's [67] equation for a bimetallic strip if the thermal strain $(\alpha_f - \alpha_s)\delta T$ is replaced by the misfit strain Δ induced by the amorphization:

$$\kappa = \frac{6}{t} \frac{2 + (r_t + r_t^{-1})}{6 + 4(r_t + r_t^{-1}) + (r_E r_t^2 + r_E^{-1} r_t^{-2})} \Delta, \quad (\text{C1})$$

where κ is the reciprocal of the bending radius, r_E and r_t are the ratios of the Young's moduli and layer thicknesses, and t is the total thickness. This equation becomes insensitive to r_t

or r_E if they are both near unity, in which case $\kappa \approx \frac{3\Delta}{2t}$. Refer to the Supplemental Material for Eq. (C1) derivation details [34].

We measured the bending radius for cantilevers that were anchored only on one side as a function of Ga^+ dose D for different energies such as 10 and 30 keV (Fig. 9). At these energies, the average penetration depths of ions in silicon are ~ 12 and 26 nm, respectively, as determined from SUSPRE analytical calculations [28]. In both cases, we find that κ increases linearly with dose after a threshold dose [Fig. 9(d)]. In the case of 10 keV, the threshold is $\sim 1 \times 10^{15}$ to 1.4×10^{15} cm^{-2} , whereas for 30 keV, the threshold is $< 4 \times 10^{14}$ cm^{-2} . Above the threshold, the linear relationship is approximately proportional (i.e., the intercept, though nonzero, is small), suggesting that, under these conditions, the dose controls Δ , while either r_E and r_t are reasonably constant and independent of D , or they are near unity so that κ is approximately

independent of them. In the case of ions of intermediate energy, 20 keV, the curvature κ is very large even for the lowest doses. Based on Eq. (C1), κ goes through a maximum when r_t goes through unity, and we infer that, while the dose primarily controls Δ , the energy mainly controls r_t , which is consistent with the SUSPRE results, as in Fig. 9(e). Finally, we found that the implanted species used is also important. We produced circular tympana of fixed size ($a = 17.5$) and corresponding amorphization dose but with different species and energy. As expected from the cantilever measurements just mentioned, the induced strain increases for Ga^+ when reducing the energy from 30 to 20 keV, as per Fig. 9(f). However, the strain increases when replacing 30 keV Ga^+ with 30 keV Xe^+ . We attribute the higher strain achieved by the Xe^+ implants to the higher damage cloud produced by a larger ion, the higher electronic energy loss after the implantation event, and the fact that, unlike the gaseous species (Xe), the metallic species Ga stays in interstitial positions, causing a mild expansion of the crystal lattice [28]. Thus, by carefully choosing the dose, the beam energy, and the implanted species, it seems likely that even higher strain values might be achievable.

Taking the linear part of the curvature to dose data on Fig. 9(d) for the 30 keV Ga^+ experiment, the slope of the experimental κ vs D is $0.008 \mu\text{m}^{-1}$ per 10^{14} ions cm^{-2} ,

and assuming that $\kappa \approx \frac{3\Delta}{2t}$, the implied misfit strain for $t = 0.035 \mu\text{m}$ is $\Delta/D = 0.00020$ per 10^{14} ions $\text{cm}^{-2} = 0.020\%$ per 10^{14} ions cm^{-2} . Therefore, for $D = 5 \times 10^{14}$ ions cm^{-2} [as used in Fig. 9(f), red colored plot], the misfit strain is $\Delta = 0.1\%$. Recall that Δ is the misfit strain in the bilayer, i.e., the fractional difference in the natural lengths of the top and bottom materials in the bilayer (a-Si and c-Si, respectively). Such a tiny misfit strain in the tensioner would not be expected to be capable of inducing strains of several percent in the tympanum if it were not for the large amplification by the geometrical factor from the relative areas of the tensioner and tympanum. This observation also indicates that, although easily controllable, the proposed method creates a very complex through-thickness system based on a mix of defects created by the ion collision cascade and the penetration distribution. Several attempts to model this system via finite element analysis have been carried out, but none reproduces even the simplest case of the cantilever bending. Therefore, we use Timoshenko's approximation to predict optimum ion beam energy and species and as a way to highlight the nonconventional mechanics involved in this system, which is closer to a ribbon curling [68] created by several nanometer-sized blades at the point of each line scan (i.e., 10 nm apart from each other).

-
- [1] M. J. Süess, R. Geiger, R. A. Minamisawa, G. Schiefler, J. Frigerio, D. Chrastina, G. Isella, R. Spolenak, J. Faist, and H. Sigg, Analysis of enhanced light emission from highly strained germanium microbridges, *Nat. Photonics* **7**, 466 (2013).
- [2] S. J. Sweeney, T. D. Eales, and A. R. Adams, The impact of strained layers on current and emerging semiconductor laser systems, *J. Appl. Phys.* **125**, 82538 (2019).
- [3] N. Healy, S. Mailis, N. M. Bulgakova, P. J. A. Sazio, T. D. Day, J. R. Sparks, H. Y. Cheng, J. V. Badding, and A. C. Peacock, Extreme electronic bandgap modification in laser-crystallized silicon optical fibres, *Nat. Mater.* **13**, 1122 (2014).
- [4] E. M. T. Fadaly, A. Dijkstra, J. R. Suckert, D. Ziss, M. A. J. van Tilburg, C. Mao, Y. Ren, V. T. van Lange, K. Korzun, and S. Kölling, Direct-bandgap emission from hexagonal Ge and SiGe alloys, *Nature (London)* **580**, 205 (2020).
- [5] J. R. Jain, A. Hryciw, T. M. Baer, D. A. B. Miller, M. L. Brongersma, and R. T. Howe, A micromachining-based technology for enhancing germanium light emission via tensile strain, *Nat. Photonics* **6**, 398 (2012).
- [6] F. T. A. Pilon, A. Lyasota, Y.-M. Niquet, V. Reboud, V. Calvo, N. Pauc, J. Widiez, C. Bonzon, J.-M. Hartmann, and A. Chelnokov, Lasing in strained germanium microbridges, *Nat. Commun.* **10**, 2724 (2019).
- [7] R. Geiger, T. Zabel, E. Marin, A. Gassenq, J.-M. Hartmann, J. Widiez, J. Escalante, K. Guillois, N. Pauc, and D. Rouchon, Uniaxially stressed germanium with fundamental direct band gap, [arXiv:1603.03454](https://arxiv.org/abs/1603.03454).
- [8] P. Vogl, M. M. Rieger, J. A. Majewski, and G. Abstreiter, How to convert group-IV semiconductors into light emitters, *Phys. Scr.* **1993**, 476 (1993).
- [9] F. Zhang, V. H. Crespi, and P. Zhang, Prediction that Uniaxial Tension Along $\langle 111 \rangle$ Produces a Direct Band Gap in Germanium, *Phys. Rev. Lett.* **102**, 156401 (2009).
- [10] D. Shiri, Y. Kong, A. Buin, and M. P. Anantram, Strain induced change of bandgap and effective mass in silicon nanowires, *Appl. Phys. Lett.* **93**, 73114 (2008).
- [11] M. M. Roberts, L. J. Klein, D. E. Savage, K. A. Slinker, M. Friesen, G. Celler, M. A. Eriksson, and M. G. Lagally, Elastically relaxed free-standing strained-silicon nanomembranes, *Nat. Mater.* **5**, 388 (2006).
- [12] W. Lee, Y. Hwangbo, J.-H. Kim, and J.-H. Ahn, Mobility enhancement of strained Si transistors by transfer printing on plastic substrates, *NPG Asia Mater.* **8**, e256 (2016).
- [13] K. Uchida, A. Kinoshita, and M. Saitoh, Carrier transport in (110) nMOSFETs: subband structures, non-parabolicity, mobility characteristics, and uniaxial stress engineering, in *2006 International Electron Devices Meeting (IEEE, San Francisco, 2006)*, pp. 1–3.
- [14] R. A. Minamisawa, M. J. Süess, R. Spolenak, J. Faist, C. David, J. Gobrecht, K. K. Bourdelle, and H. Sigg, Top-down fabricated silicon nanowires under tensile elastic strain up to 4.5%, *Nat. Commun.* **3**, 1096 (2012).
- [15] A. Benyagoub, S. Löffler, M. Rammensee, S. Klaumünzer, and G. Saemann-Ischenko, Plastic deformation in SiO_2 induced by heavy-ion irradiation, *Nucl. Instrum. Methods Phys. Res. B* **65**, 228 (1992).
- [16] T. Van Dillen, A. Polman, W. Fukarek, and A. Van Blaaderen, Energy-dependent anisotropic deformation of colloidal silica particles under MeV Au irradiation, *Appl. Phys. Lett.* **78**, 910 (2001).
- [17] W. J. Arora, H. I. Smith, and G. Barbastathis, Membrane folding by ion implantation induced stress to fabricate three-

- dimensional nanostructures, *Microelectron. Eng.* **84**, 1454 (2007).
- [18] W. J. Arora, S. Sijbrandij, L. Stern, J. Notte, H. I. Smith, and G. Barbastathis, Membrane folding by helium ion implantation for three-dimensional device fabrication, *J. Vac. Sci. Technol. B* **25**, 2184 (2007).
- [19] Y.-R. Kim, P. Chen, M. J. Aziz, D. Branton, and J. J. Vlassak, Focused ion beam induced deflections of freestanding thin films, *J. Appl. Phys.* **100**, 104322 (2006).
- [20] M. J. Samayoa, M. A. Haque, and P. H. Cohen, Focused ion beam irradiation effects on nanoscale freestanding thin films, *J. Micromech. Microeng.* **18**, 95005 (2008).
- [21] S. E. Donnelly, F. Bodart, K. M. Barfoot, R. Werz, and R. P. Webb, Helium ion bombardment of thin aluminium films, *Thin Solid Films* **94**, 289 (1982).
- [22] Z. Liu, H. Du, J. Li, L. Lu, Z.-Y. Li, and N. X. Fang, Nanokirigami with giant optical chirality, *Sci. Adv.* **4**, eaat4436 (2018).
- [23] W. L. Ng, M. A. Lourenco, R. M. Gwilliam, S. Ledain, G. Shao, and K. P. Homewood, An efficient room-temperature silicon-gated light-emitting diode, *Nature (London)* **410**, 192 (2001).
- [24] I. H. Wilson, J. B. Xu, R. A. B. Devine, and R. P. Webb, Energetic ion impacts on quartz surfaces: A study by atomic force microscopy, *Nucl. Instrum. Methods Phys. Res. B* **118**, 473 (1996).
- [25] R. A. B. Devine, Macroscopic and microscopic effects of radiation in amorphous SiO₂, *Nucl. Instrum. Methods Phys. Res. B* **91**, 378 (1994).
- [26] J. Washburn, C. S. Murty, D. Sadana, P. Byrne, R. Gronsky, N. Cheung, and R. Kilaas, The crystalline to amorphous transformation in silicon, *Nucl. Instrum. Methods Phys. Res.* **209-210**, 345 (1983).
- [27] R. P. Webb, SUSPRE, <https://uknibc.co.uk/SUSPRE/>.
- [28] R. P. Webb and I. H. Wilson, An extension to the projected range algorithm (PRAL) to give energy deposition profiles, in *Proc. 2nd Int. Conf. Simulation of Semiconductor Devices and Processes* (Pine Ridge Press, Swansea, 1986), Vol. 2, p. 247.
- [29] A. Shchepetov, M. Prunnila, F. Alzina, L. Schneider, J. Cuffe, H. Jiang, E. I. Kauppinen, C. M. Sotomayor Torres, and J. Ahopelto, Ultra-thin free-standing single crystalline silicon membranes with strain control, *Appl. Phys. Lett.* **102**, 192108 (2013).
- [30] B. Davidovitch and D. Vella, Partial wetting of thin solid sheets under tension, *Soft Matter* **14**, 4913 (2018).
- [31] F. Box, D. O'Kiely, O. Kodio, M. Inizan, A. A. Castrejón-Pita, and D. Vella, Dynamics of wrinkling in ultrathin elastic sheets, *Proc. Natl. Acad. Sci.* **116**, 20875 (2019).
- [32] E. A. Flores-Johnson, T. J. Rupert, K. J. Hemker, D. S. Gianola, and Y. Gan, Modelling wrinkling interactions produced by patterned defects in metal thin films, *Extrem. Mech. Lett.* **4**, 175 (2015).
- [33] F. Liu, F. Xu, and C. Fu, Orientable wrinkles in stretched orthotropic films, *Extrem. Mech. Lett.* **33**, 100579 (2019).
- [34] See Supplemental Material at <http://link.aps.org/supplemental/10.1103/PhysRevMaterials.5.124603> for (i) further details on the flattening of a buckled Si membrane, (ii) STEM images of circular tympana used, (iii) bimaterial bending formalism, which includes Refs. [69–72].
- [35] M. J. Suess, R. A. Minamisawa, R. Geiger, K. K. Bourdelle, H. Sigg, and R. Spolenak, Power-dependent Raman analysis of highly strained Si nanobridges, *Nano Lett.* **14**, 1249 (2014).
- [36] A. S. Nikolenko, Laser heating effect on Raman spectra of Si nanocrystals embedded into SiO_x matrix, *Semicond. Phys. Quantum Electron. Optoelectron.* **16**, 86 (2013).
- [37] F. Adar, E. Lee, S. Mamedov, and A. Whitley, Experimental evaluation of the depth resolution of a Raman microscope, *Microsc. Microanal.* **16**, 360 (2010).
- [38] S. Ganesan, A. A. Maradudin, and J. Oitmaa, A lattice theory of morphic effects in crystals of the diamond structure, *Ann. Phys. (N. Y.)* **56**, 556 (1970).
- [39] E. Anastassakis, A. Cantarero, and M. Cardona, Piezo-Raman measurements and anharmonic parameters in silicon and diamond, *Phys. Rev. B* **41**, 7529 (1990).
- [40] E. Anastassakis, A. Pinczuk, E. Burstein, F. H. Pollak, and M. Cardona, Effect of static uniaxial stress on the Raman spectrum of silicon, *Solid State Commun.* **88**, 1053 (1993).
- [41] I. De Wolf, Stress measurements in Si microelectronics devices using Raman spectroscopy, *J. Raman Spectrosc.* **30**, 877 (1999).
- [42] C.-Y. Peng, C.-F. Huang, Y.-C. Fu, Y.-H. Yang, C.-Y. Lai, S.-T. Chang, and C. W. Liu, Comprehensive study of the Raman shifts of strained silicon and germanium, *J. Appl. Phys.* **105**, 83537 (2009).
- [43] F. Ureña, S. H. Olsen, and J.-P. Raskin, Raman measurements of uniaxial strain in silicon nanostructures, *J. Appl. Phys.* **114**, 144507 (2013).
- [44] F. Cerdeira, C. J. Buchenauer, F. H. Pollak, and M. Cardona, Stress-induced shifts of first-order Raman frequencies of diamond and zinc-blende-type semiconductors, *Phys. Rev. B* **5**, 580 (1972).
- [45] A. Gassenq, S. Tardif, K. Guilloy, G. Osvaldo Dias, N. Pauc, I. Duchemin, D. Rouchon, J.-M. Hartmann, J. Widiez, and J. Escalante, Accurate strain measurements in highly strained Ge microbridges, *Appl. Phys. Lett.* **108**, 241902 (2016).
- [46] A. Gassenq, S. Tardif, K. Guilloy, I. Duchemin, N. Pauc, J. M. Hartmann, D. Rouchon, J. Widiez, Y. M. Niquet, and L. Milord, Raman-strain relations in highly strained Ge: Uniaxial (100), (110) and biaxial (001) stress, *J. Appl. Phys.* **121**, 55702 (2017).
- [47] J. Macia, E. Martín, A. Pérez-Rodríguez, J. Jimenez, J. R. Morante, B. Aspar, and J. Margail, Raman microstructural analysis of silicon-on-insulator formed by high dose oxygen ion implantation: As-implanted structures, *J. Appl. Phys.* **82**, 3730 (1997).
- [48] D. C. Cox, *Introduction to Focused Ion Beam Nanometrology* (Morgan & Claypool Publishers, San Rafael, California (USA), 2015).
- [49] C. Lehrer, L. Frey, S. Petersen, and H. Ryssel, Limitations of focused ion beam nanomachining, *J. Vac. Sci. Technol. B* **19**, 2533 (2001).
- [50] L. Frey, C. Lehrer, and H. Ryssel, Nanoscale effects in focused ion beam processing, *Appl. Phys. A* **76**, 1017 (2003).
- [51] M. K. Sahoo and P. G. Kale, Micro-Raman study of growth parameter restraint for silicon nanowire synthesis using MACE, *Superlattices Microstruct.* **135**, 106289 (2019).
- [52] A. Winkelmann and G. Nolze, Analysis of Kikuchi band contrast reversal in electron backscatter diffraction patterns of silicon, *Ultramicroscopy* **110**, 190 (2010).
- [53] H. Nagai, Anisotropic bending during epitaxial growth of mixed crystals on GaAs substrate, *J. Appl. Phys.* **43**, 4254 (1972).

- [54] G. Stan, S. Krylyuk, A. V. Davydov, I. Levin, and R. F. Cook, Ultimate bending strength of Si nanowires, *Nano Lett.* **12**, 2599 (2012).
- [55] H. Zhang, J. Tersoff, S. Xu, H. Chen, Q. Zhang, K. Zhang, Y. Yang, C.-S. Lee, K.-N. Tu, and J. Li, Approaching the ideal elastic strain limit in silicon nanowires, *Sci. Adv.* **2**, e1501382 (2016).
- [56] V. Reboud, A. Gassenq, J. M. Hartmann, J. Widiez, L. Viro, J. Aubin, K. Guillo, S. Tardif, J. M. Fédéli, and N. Pauc, Germanium based photonic components toward a full silicon/germanium photonic platform, *Prog. Cryst. Growth Charact. Mater.* **63**, 1 (2017).
- [57] J. A. Rogers, M. G. Lagally, and R. G. Nuzzo, Synthesis, Assembly and Applications of Semiconductor Nanomembranes, *Nature (London)* **477**, 45 (2011).
- [58] V. Mondiali, M. Lodari, M. Borriello, D. Chrastina, and M. Bollani, Top-down SiGe nanostructures on Ge membranes realized by e-beam lithography and wet etching, *Microelectron. Eng.* **153**, 88 (2016).
- [59] Q. M. Thai, N. Pauc, J. Aubin, M. Bertrand, J. Chrétien, A. Chelnokov, J. M. Hartmann, V. Reboud, and V. Calvo, 2D hexagonal photonic crystal GeSn laser with 16% Sn content, *Appl. Phys. Lett.* **113**, 51104 (2018).
- [60] M. R. M. Atalla, S. Assali, A. Attiaoui, C. Lemieux-Leduc, A. Kumar, S. Abdi, and O. Moutanabbir, All-group IV transferable membrane mid-infrared photodetectors, *Adv. Funct. Mater.* **31**, 2006329 (2021).
- [61] H. Jansen, H. Gardeniers, M. de Boer, M. Elwenspoek, and J. Fluitman, A survey on the reactive ion etching of silicon in microtechnology, *J. Micromech. Microeng.* **6**, 14 (1996).
- [62] A. Witvrouw, B. Du Bois, P. De Moor, A. Verbist, C. A. Van Hoof, H. Bender, and C. Baert, Comparison between wet HF etching and vapor HF etching for sacrificial oxide removal, in *Micromachining and Microfabrication Process Technology VI*, Vol. 4174 (International Society for Optics and Photonics, Santa Clara, 2000), pp. 130–141.
- [63] Q. Vu, D. A. Stricker, and P. M. Zavracky, Surface characteristics of (100) silicon anisotropically etched in aqueous KOH, *J. Electrochem. Soc.* **143**, 1372 (1996).
- [64] J. P. Biersack, New projected range algorithm as derived from transport equations, *Z. Physik A* **305**, 95 (1982).
- [65] J. P. Biersack, Calculation of projected ranges—analytical solutions and a simple general algorithm, *Nucl. Instrum. Methods* **182-183**, 199 (1981).
- [66] A. J. Wilkinson, G. Meaden, and D. J. Dingley, High-resolution elastic strain measurement from electron backscatter diffraction patterns: New levels of sensitivity, *Ultramicroscopy* **106**, 307 (2006).
- [67] S. Timoshenko, Analysis of bi-metal thermostats, *Josa* **11**, 233 (1925).
- [68] C. Prior, J. Moussou, B. Chakrabarti, O. E. Jensen, and A. Juel, Ribbon curling via stress relaxation in thin polymer films, *Proc. Natl. Acad. Sci.* **113**, 1719 (2016).
- [69] K. Brunner, G. Abstreiter, B. O. Kolbesen, and H. W. Meul, Strain at Si-SiO₂ interfaces studied by micron-Raman spectroscopy, *Appl. Surf. Sci.* **39**, 116 (1989).
- [70] R. J. Jaccodine and W. A. Schlegel, Measurement of strains at Si-SiO₂ interface, *J. Appl. Phys.* **37**, 2429 (1966).
- [71] G. Taraschi, A. J. Pitera, and E. A. Fitzgerald, Strained Si, SiGe, and Ge on-insulator: Review of wafer bonding fabrication techniques, *Solid. State. Electron.* **48**, 1297 (2004).
- [72] D. B. Williams and C. B. Carter, *Transmission Electron Microscopy: A Textbook for Materials Science* (Plenum Press, New York, 1996).